nature physics

ARTICLES

https://doi.org/10.1038/s41567-018-0154-4

Physical forces determining the persistency and centring precision of microtubule asters

Hirokazu Tanimoto[1,2], Jeremy Sallé[1], Louise Dodin[1] and Nicolas Minc[1*]

In early embryos, microtubules form star-shaped aster structures that can measure up to hundreds of micrometres in size, and move at high speeds to find the geometrical centre of the cell. This process, known as aster centration, is essential for the fidelity of cell division and development, but how cells succeed in moving these large structures through their crowded and fluctuating cytoplasm remains unclear. Here, we demonstrate that the positional fluctuations of migrating sea urchin sperm asters are small, anisotropic, and associated with the stochasticity of dynein-dependent forces moving the aster. Using in vivo magnetic tweezers to directly measure aster forces inside cells, we derive a linear aster force–velocity relationship and provide evidence for a spring-like active mechanism stabilizing the transverse position of the asters. The large frictional coefficient and spring constant quantitatively account for the amplitude and growth characteristics of athermal positional fluctuations, demonstrating that aster mechanics ensure noise suppression to promote persistent and precise centration. These findings define generic biophysical regimes of active cytoskeletal mechanics underlying the accuracy of cell division and early embryonic development.

Microtubule asters are star-shaped cytoskeletal structures composed of microtubule polymers radiating from an organizing centre called the centrosome. They contribute to the spatial organization of crucial functions in eukaryotic cells, ranging from cell migration to nuclear centration and mitotic spindle orientation[1–3]. One highly conserved property of microtubule asters is their ability to probe the geometrical boundaries of the cell to move and position themselves in the exact cell centre. This was best highlighted in seminal in vitro work reconstituting aster growth and centration in microfabricated wells of a few micrometres in size. In those studies, pushing forces resulting from astral microtubule polymerization against the chamber wall[4,5] or pulling forces provided by minus-end directed dynein motors attached to the wall surface[6] allowed asters to target the chamber centre.

A stereotypical and ubiquitous in vivo counterpart for aster centration occurs soon after fertilization in most animal embryos[7]. In this context, the fertilizing sperm brings the male pro-nucleus and its associated centrosomal material into the side of the egg, which results in the nucleation of a 'sperm aster' that continuously grows and moves to the egg centre. This centration motion is critical to position the nucleus and subsequent spindle and division plane in the exact cell centre. Contrary to in vitro situations, studies in systems including worm, frog, fish and echinoderm embryos have suggested that aster centration in those cells may not primarily involve microtubule polymerization or cortical dynein forces[8–12]. Rather, a prominent model is that most of the forces are provided by dynein motors working along astral microtubules in bulk cytoplasm[11,13–15]. Dynein motors generate plus-end directed traction forces, probably as complexes with endomembrane components such as the endoplasmic reticulum, lysosome vesicles or yolk granules[13,14], via frictional interactions with the viscous cytoplasm. As longer microtubules may associate with more cargos, they may exert larger pulling forces on the centrosome. This length-dependent system, coupled to microtubule length asymmetries caused by cellular boundaries, provides a self-organization design for asters to target the cell centre[11,15–17].

One outstanding physical problem posed by aster centration in early embryos arises from the unusually large size of egg cells and early blastomeres[3,18]. These cells are typically 10–100 times larger than somatic cells[19] or in vitro microchambers[6], yet achieve aster centration on a timescale of only a few tens of minutes. Because of the physiological importance of aster centration in early embryos, these parameters set extreme constraints on motion persistency, speed and centring precision. Given cytoplasmic crowding, extrinsic cellular noise, and intrinsic stochasticity of molecular elements involved[20,21], how moving asters may satisfy those constraints inside cells remains mysterious overall.

Here we exploited the centration of sea urchin sperm asters as a quantitative model system to derive the biophysical principles ensuring robust aster centration. By combining high-resolution tracking and direct intracellular aster force measurement, we find that aster motion is associated with large forces and small active positional fluctuations. This work demonstrates how aster mechanics may ensure noise suppression to promote persistent and precise centration.

We first employed high-resolution microscopy (spatial resolution ~20 nm, temporal resolution ~50 ms, see Methods) (Supplementary Fig. 1–2 and Supplementary Movie 1) to track the motion of male pro-nuclei attached to sperm microtubule asters in fertilized sea urchin eggs. We confirmed that aster speed was, on average, constant along the longitudinal centring direction (X axis) and zero along the transverse axis (Y axis)[11]. Aster trajectory appeared smooth overall, but did exhibit some minor excursions away from the centring axis, which rapidly resorbed (Fig. 1a,b).

To quantitatively examine the stochastic fluctuations around the mean motion, we detrended aster trajectory by subtracting its local velocity and computed the residual displacements, δX and δY, as a function of lag time, δt (equation 5)[22]. The probability distribution functions (PDFs) of δX and δY were nearly similar for $\delta t < 30$ sec, and were well described by Gaussian functions (Fig. 1c). For $\delta t > 30$ sec, whereas the PDF of δY kept a near-constant shape, the PDF of δX appeared to deviate from a Gaussian and had a

[1]Institut Jacques Monod, CNRS UMR7592 and Université Paris Diderot, Paris , France. [2]Present address: Department of Materials Science, Yokohama City University, Yokohama, Japan. *e-mail: nicolas.minc@ijm.fr

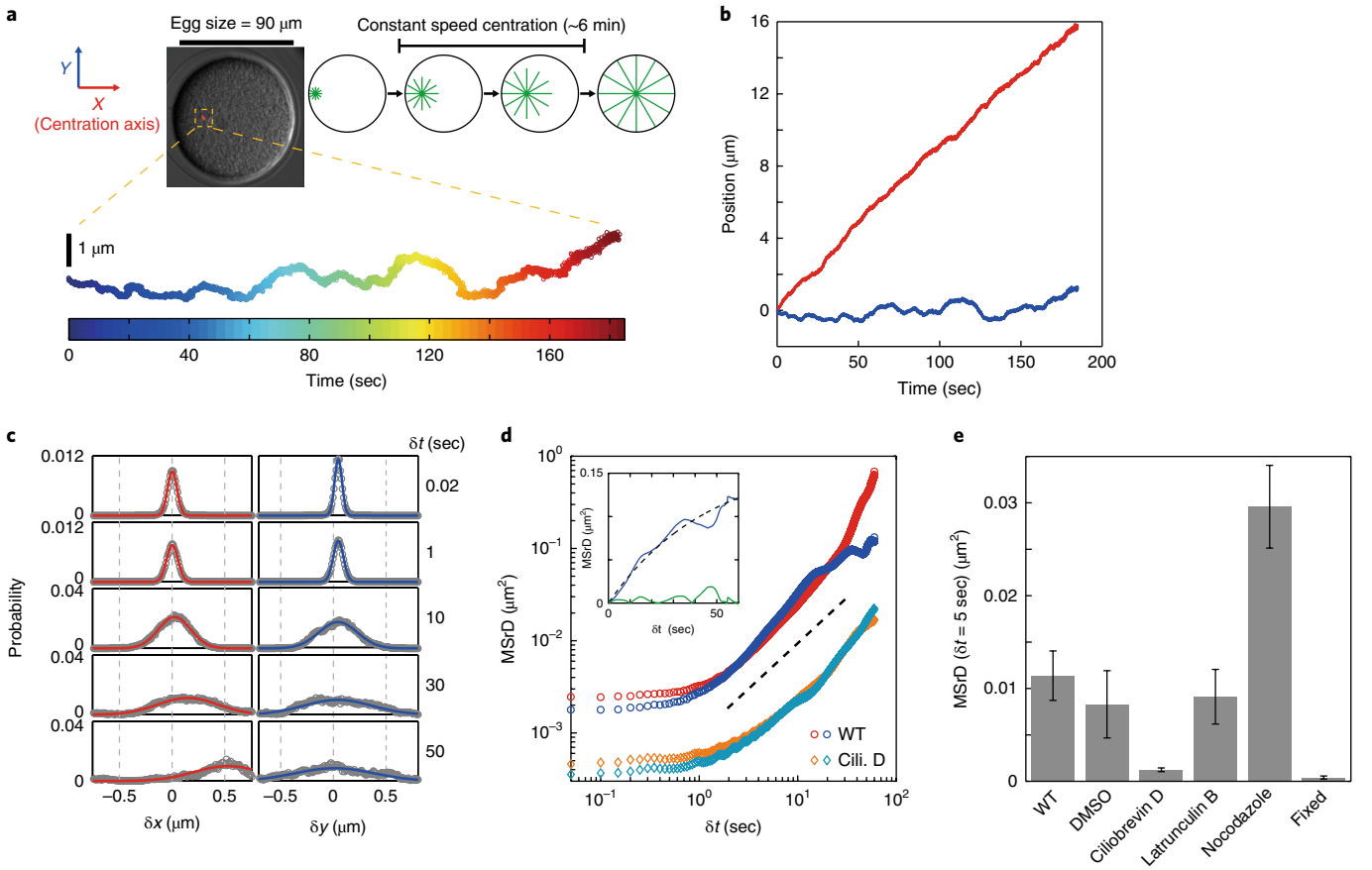

Fig. 1 | Fluctuation analysis of centring microtubule asters. a,**b**, High-resolution tracking of sperm microtubule asters during the constant-speed centration phase. The representative 3 min trajectory corresponds to 3,600 time points. Aster *XY* position was defined using *X* as the centring axis. **c**, PDFs of residual displacements along *X* and *Y* for different δ*t*. Bold lines are best-fit Gaussian distributions. **d**, *X* and *Y* MSrDs for control and Ciliobrevin D-treated samples plotted as a function of δ*t* on a log scale. The broken line indicates a slope of 1. Inset: transverse MSrD (blue curve) of controls superimposed with a fit of the model from equation 1 (broken line), plotted on a linear scale. The absolute magnitude of the residual error between the fit and the data is also depicted (green curve). **e**, Contributions of cytoskeletal components to aster positional fluctuations. The fluctuation amplitude was characterized by computing the MSrD at $\delta t = 5$ sec. WT (wild-type) corresponds to untreated eggs. Error bars represent standard deviations.

non-zero mean, which could reflect more complex behaviours such as higher-order slow changes in the aster mean speed.

We characterized the statistical properties of aster fluctuations by plotting the second-order moment of δ*X* and δ*Y* (mean-squared residual displacement, MSrD) as a function of δ*t* (Fig. 1d). Both MSrDs were flat at $\delta t < 1$ sec, due to measurement noise. They then grew linearly above the measurement noise with a slope close to 1 for $1 < \delta t < 30$ sec, suggesting diffusive dynamics with similar diffusion coefficients along both axes: $D_x = 1.7\times10^{-3}\,\mu m^2\,sec^{-1}$ and $D_y = 1.8\times10^{-3}\,\mu m^2\,sec^{-1}$. These results indicate the existence of uniform random forces which cause asters to fluctuate in a diffusive manner.

The two MSrDs had different behaviours at $\delta t > 30$ sec. Whereas the longitudinal fluctuations kept growing, the transverse fluctuations saturated, probably reflecting a positional feedback that stabilizes the aster trajectory transversely (Fig. 1d). Accordingly, these transverse fluctuations were described well by a random walk under spring-like restoration forces (Fig. 1d, inset)[23], so that

$$\mathrm{MSrD}_y(\delta t) = 2\tau D_y\,(1-e^{-\delta t/\tau}) \qquad (1)$$

with a saturation amplitude $2\tau D_y = 0.17\,\mu m^2$ and saturation timescale $\tau = 46$ sec. This corresponded to the typical size and restoration time of excursion events away from the centring axis. The saturation amplitude allowed an estimation of the mean deviation distance of the aster from the centring axis of $\sqrt{2\tau D_y} = 0.41\,\mu m$, which was typically less than 1% of the cell radius, demonstrating a remarkable centration precision. Thus, aster fluctuations are small and anisotropic, with characteristics determined by a balance between random forces and viscous dampening, and additional spring-like feedback in the transverse axis.

To discern if the observed fluctuations reflected thermal noise or active processes, we manipulated cytoskeletal components using specific chemical inhibitors (Fig. 1d,e and Supplementary Figs. 3–4). To separately characterize the diffusive fluctuations from the effects of positional feedback, we computed a fluctuation amplitude defined as MSrD at $\delta t = 5$ sec, where asters exhibit purely diffusive behaviour. Strikingly, the addition of 100 μM of Ciliobrevin D, which inhibits dynein activity and halts aster motion without grossly altering aster growth and morphology[11] (Supplementary Fig. 3), decreased the positional fluctuation amplitude by almost an order of magnitude. Thus, dynein force-generation events which drive aster centration may also add active noise to this motion because of their stochastic nature. Actin depolymerization with 20 μM Latrunculin B affected cell cortex and cell shape[11], but did not affect aster motion or fluctuation amplitude. This suggests that dynein drives aster fluctuations within the bulk cytoplasm, not from the cortex, and by associating with cytoplasmic elements independent of actin[23,24]. Finally, treatment with 20 μM Nocodazole

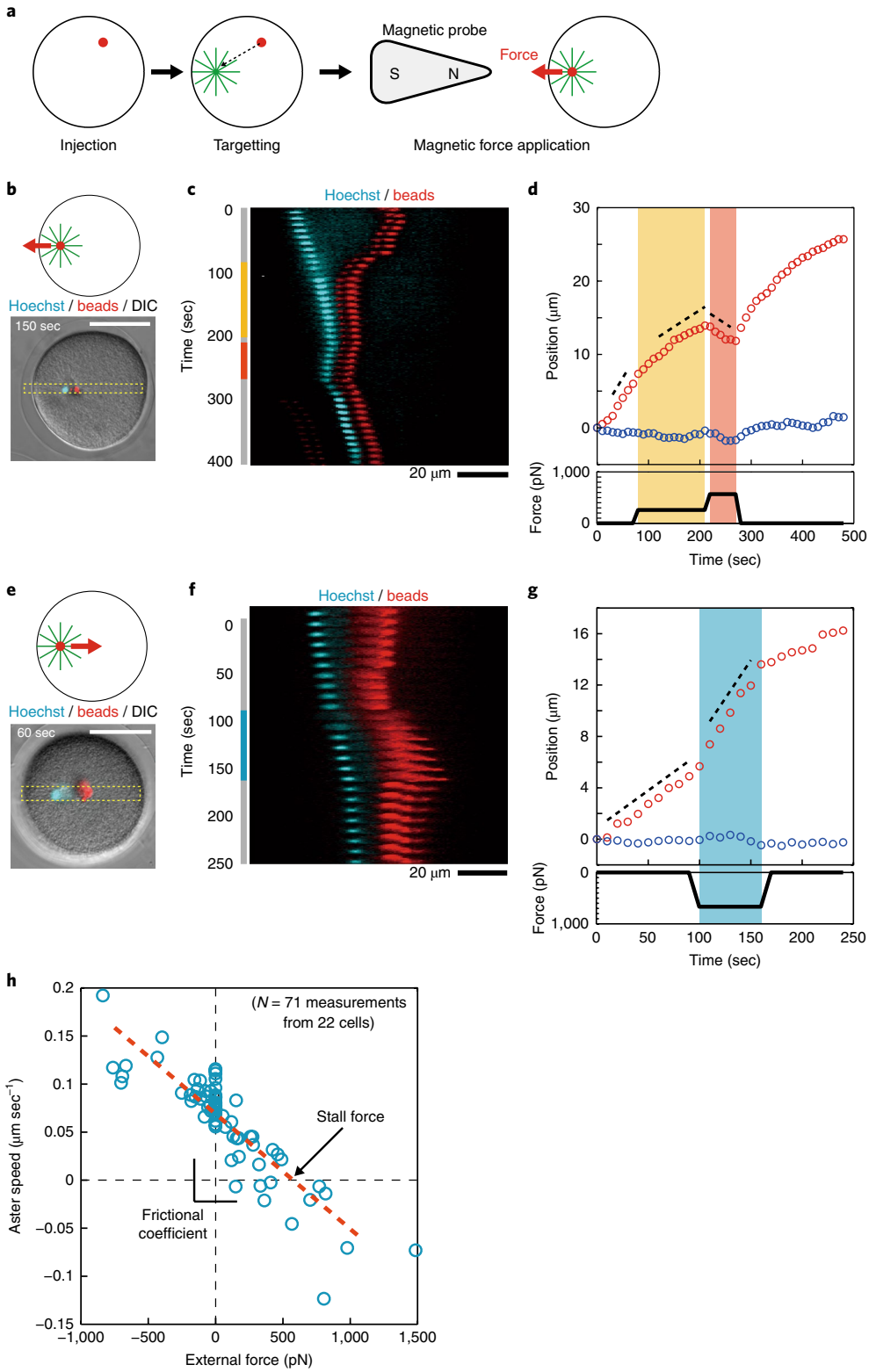

Fig. 2 | Force–velocity relationships of microtubule asters. a, Aggregates of injected magnetic beads were targeted to the aster centre to directly apply magnetic forces to centring asters. **b**–**g**, External magnetic forces were applied to asters either against (**b**–**d**) or along (**e**–**g**) the centring direction. The 1D kymographs (**c** and **f**) and time-evolution of aster *XY* positions (**d** and **g**) show how applied forces consistently change aster longitudinal speed. DIC, differential interference contrast. **h**, Aster longitudinal speed V_x plotted as a function of external force amplitude. $N = 71$ measurements from 22 cells. The red broken line indicates a linear fit.

to depolymerize microtubules also halted aster motion, but caused the sperm nucleus to fluctuate more than in controls, suggesting that microtubules may contribute to a large fraction of aster viscous drag. Importantly, in Nocodazole and Ciliobrevin D treatments, longitudinal and transverse MSrDs both grew diffusively for the entire timescale without saturation (Fig. 1d and Supplementary Fig. 4).

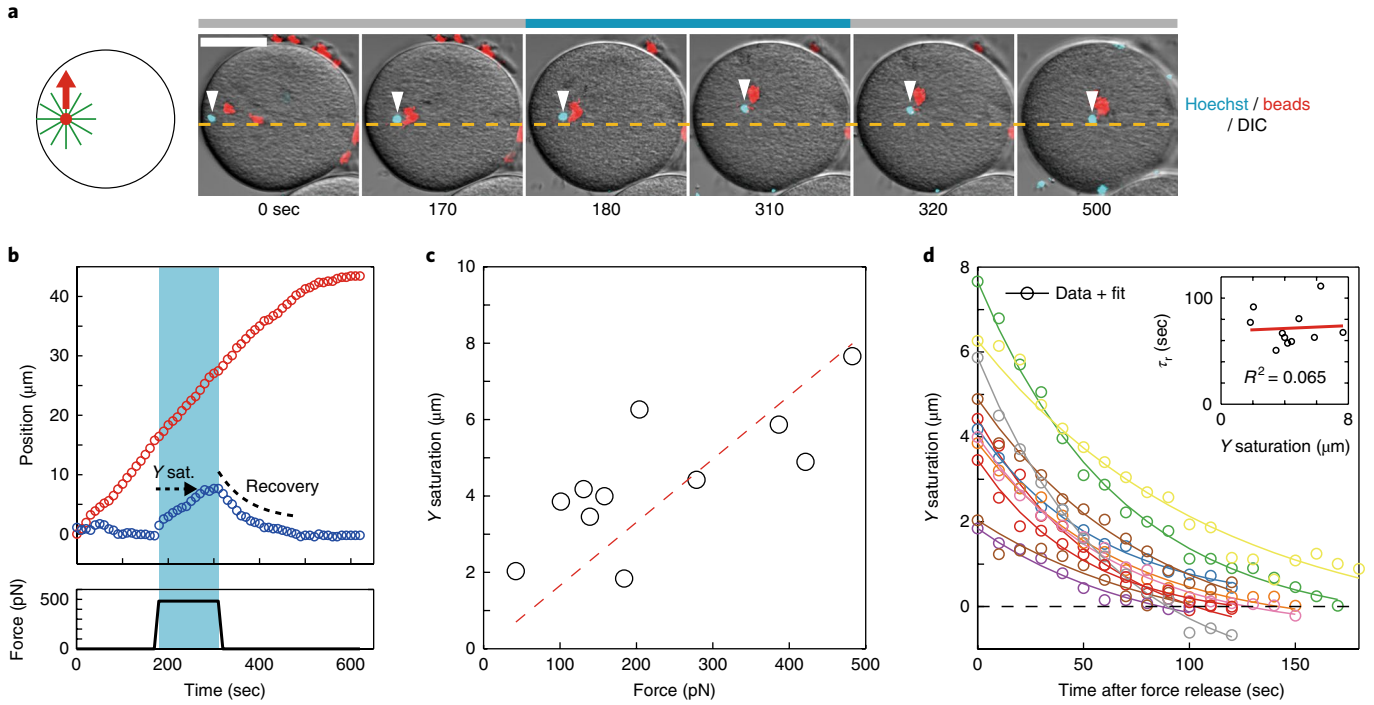

Fig. 3 | Direct demonstration of a transverse feedback stabilizing asters along their centring direction. a,**b**, External forces were applied orthogonally to the centring direction along the *Y* axis for 140 sec. The applied force causes a drift towards the magnet tip. **c**, Aster *Y* saturation (shown in **b**) plotted as a function of external force amplitude. $N=10$ measurements from 10 cells. The spring constant $\kappa=59\,\mathrm{pN\,\mu m^{-1}}$ was determined from the slope of the linear fit (red broken line). **d**, Recovery dynamics of aster *Y* position. Aster *Y* position after force cessation was plotted as a function of time. $N=10$ measurements from 10 cells. Solid lines indicate best fits with an exponential function (equation S6), yielding a mean recovery timescale $\tau_r=72+/-18$ sec. Inset: Recovery timescale plotted as a function of *Y* saturation. The correlation analysis indicates that there is no correlation between the two variables.

This indicates that microtubules and dynein contribute to the transverse spring-like feedback.

To understand how those kinetic properties may emerge from the mechanical properties of moving asters, we set out to directly measure the physical forces of asters inside cells. We modified a magnetic tweezer strategy recently used to measure forces for mitotic spindle maintenance in *Caenorhabditis elegans*[25] to be able to apply larger forces of several hundreds of piconewtons to moving asters in arbitrary directions. These modifications rested on the injection of magnetic beads with highly persistent minus-end targeting activity, which rapidly aggregated and bound to the aster centre after fertilization in a microtubule- and dynein-dependent manner[26]. Application of large calibrated forces was achieved by bringing a sharpened steel piece connected to a magnet to a controlled distance from the internalized beads (Fig. 2a and Supplementary Figs. 5–9) (see Supplementary Information).

Application of external longitudinal forces against aster-centring motion caused aster speed to decrease in a dose-dependent manner (Fig. 2b–d, Supplementary Fig. 10 and Supplementary Movie 2). In these experiments, we focused on a short-timescale response by computing aster speed within typically ~ 30 sec after force application, to minimize long-term adaptive responses. In Fig. 2b–d, we first applied a 260 pN force, which dropped the aster longitudinal speed V_x by almost a factor of two without altering V_y. This force was subsequently increased to 570 pN, which further decreased V_x to a negative value, thus reverting aster motion. After the force was released, the aster restored a centring velocity close to its original value, suggesting that external forces did not grossly perturb aster organization. Conversely, applying external forces along the centring direction caused asters to accelerate (Fig. 2e–g, Supplementary Fig. 11 and Supplementary Movie 3). In Fig. 2e–g, we applied a 670 pN force in the positive *X* direction which increased aster speed by nearly twofold.

Systematic repetition of these measurements allowed the derivation of an aster force–velocity relationship for a wide range of external forces, from +1,500 pN to −700 pN (a positive force corresponds to a rear pull). Consequent changes in longitudinal aster speed V_x varied from −0.13 to 0.2 μm sec^{-1} and collapsed into a single linear curve (Fig. 2h and Supplementary Fig. 12). These results indicate that aster motion is governed by a simple linear friction law, so that

$$V_x=\frac{1}{\gamma}(F_{\mathrm{aster}}-F_{\mathrm{external}}) \qquad (2)$$

Importantly, this linear relationship holds for external forces applied along and against aster centring motion, suggesting that contributions from compressive microtubule forces at the aster rear, close to the cortex, may be negligible here. Using those results, we determined an aster stall force which is equal to the aster endogenous force of $F_{\mathrm{aster}}=580+/-21$ pN, and a frictional coefficient γ of 8,400 +/− 280 pN sec μm^{-1} (+/− indicates the standard error in fitting parameters unless specified). Detached bead aggregates with a similar size to the male pro-nucleus moved much faster than asters under the same forces, indicating that most of this friction may be associated with microtubules in the aster (Supplementary Fig. 6). These results demonstrate that the centring motion of sperm asters obeys a simple linear friction law involving large self-propelling forces and drag.

Fluctuation analyses in the transverse axis supported the existence of a spring-like feedback mechanism stabilizing aster position around the centring axis. To characterize this feedback, we applied magnetic forces perpendicular to the motion direction

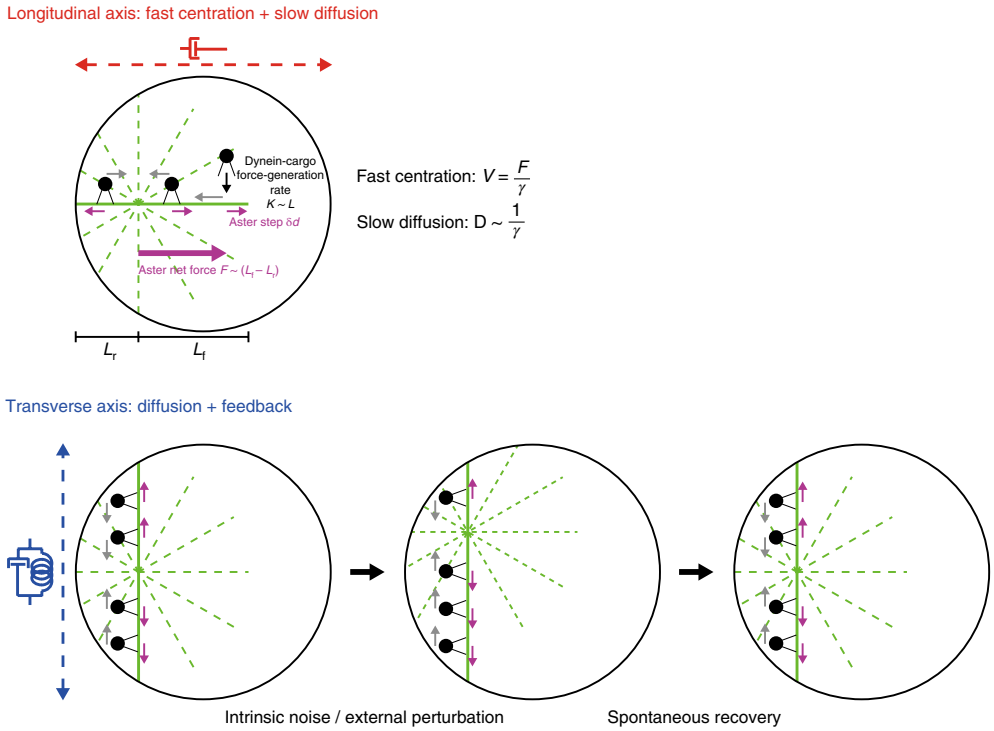

Fig. 4 | Aster mechanics ensure fast, persistent and precise aster centration. The large frictional coefficient of asters suppresses active fluctuations along the longitudinal axis. This process was analysed using a simple Poisson model, in which a single dynein-force generation event causes an aster step motion (see main text and Supplementary Information). Given this large drag, asters must exert a large net endogenous forces to move at a high speed in the cytoplasm. Along the transverse axis, fluctuations are further suppressed by a dynein-dependent feedback mechanism, which stabilizes the centring direction with respect to cell geometry.

(Fig. 3a,b, Supplementary Fig. 13 and Supplementary Movie 4). In Fig. 3a,b, we applied a 470 pN force in the positive Y direction for 140 sec. The external force did not affect aster motion along the X axis, but caused a continuous drift in Y which eventually saturated ~7 μm away from the X axis. Remarkably, after force cessation the Y position restored to its original value within tens of seconds (Fig. 3b). Computing the maximum Y displacement at saturation as a function of various applied forces yielded a linear force–displacement curve (Fig. 3c). These results directly demonstrate the existence of a linear spring stabilizing aster position around the centration axis, with a spring constant of $\kappa = 59 +/- 2.8\,\mathrm{pN\,\mu m^{-1}}$. The stiffness of this spring is approximately four times higher than in *C. elegans*[25], plausibly revealing different force-generation mechanisms. Accordingly, the transverse speed V_y following force application was comparable to the changes in V_x in the longitudinal force experiments, ruling out a major contribution of microtubule compressive forces to this transverse feedback. In addition, it has been shown that aster laser severing along the transverse axis in this system yields aster motion away from the site of ablation[11]. These data support that this centring spring is mostly associated with microtubule pulling forces.

These transverse force experiments are consistent with a Kelvin–Voigt model, in which an elastic spring and viscous dashpot are connected in parallel[25] (Fig. 4). This model predicts that the mean-squared displacement driven by internal random forces should saturate in an exponential manner, as observed in fluctuation analysis, with a timescale equal to the relaxation timescale following displacement by an external load. Accordingly, quantification of the recovery dynamics after force cessation revealed a restoring kinetic well described by an exponential relaxation with a single characteristic timescale, $\tau_r = 72 +/- 18$ sec (+/−indicates standard deviation), independent of the initial Y offset (Fig. 3d). This timescale was close to the saturation timescale observed in the transverse fluctuations ($\tau = 46$ sec), supporting the consistency between our passive and active characterizations of the transverse positional feedback. Given that fluctuation saturation depended on microtubules and dynein, these results suggest that the positional feedback maintaining the aster around the centring axis relies on dynein pulling forces on microtubules.

These findings may be consistent with the length-dependent mechanism proposed to drive aster centration in sea urchins and other embryos[8–13,15,16,27,28]. This system has the properties of an 'active spring' with respect to cell geometry: a displacement away from the cell centre yields a length imbalance on the two sides of the aster and creates a dynein-dependent restoration force proportional to the displacement[8]. During aster centration, this spring is expected to function only along the transverse axis, because microtubules reach the cortex along this axis, while front microtubules do not reach to the opposite side until the very end of centration (Fig. 4)[11]. Using the simplest linear length-dependency for microtubule forces, $F_{MT} = \alpha L_{MT}$, we can relate the spring constant κ to the length-dependency factor, α, so that $\alpha = \kappa/2$. This analysis indicates that ~30 pN forces are generated per 1 μm-depth region of the aster surface (corresponding to a volume of $5\times10^3\,\mu m^3$ for an aster radius of 20 μm). This suggests a lower bound of 100–200 dynein motors involved in moving and positioning these asters, much higher than in previous indirect estimates[15,29].

Aster mechanical properties along the two different axes appeared to be largely consistent. For asters to move to the cell centre, front microtubules should be longer than those at the back, because their growth is not restricted by the cortex. We recently estimated[11] a difference in length between front and rear microtubules of $\delta L \sim 10\,\mu m$. This would correspond to a net force of $F_{aster} = \alpha\delta L \sim 300\,pN$;

smaller yet close to the direct longitudinal force measurement calculated above. Furthermore, the relaxation timescale in the transverse force experiments allows the definition of a frictional coefficient given by $\gamma = \kappa\tau_r = 4{,}200\,\mathrm{pN\,sec\,\mu m^{-1}}$. This value is comparable to but half that obtained from direct measurements in the longitudinal axis. Because the time-window used to compute the frictional coefficient in the transverse axis (>100 sec) is larger than in the longitudinal axis (~30 sec), we envisage that the differences in γ could reflect some shape changes of the aster, which could modify the effective drag over this longer timescale. Together, these findings indicate that the viscous dampening in the transverse position is essentially the same as the drag associated with aster longitudinal centring motion, and that length-dependent dynein–microtubule forces may account for both transverse feedback and the net centring force.

The frictional coefficient of microtubule asters is remarkably high: 60 times larger than the measured value for static mitotic spindles in *C. elegans* and 15 times larger than indirect estimates for sperm asters in *C. elegans*[25,30]. This value suggests that the cell dedicates an energy of at least γV^2 ~ 1,000 ATP molecules per second for centring microtubule asters. Based on the measured cytoplasmic viscosity of fertilized sea urchin eggs[31], this friction would amount to that of an object with a hydrodynamic radius of ~440 µm, typically ~20 times larger than the aster physical radius. Such large friction may not be readily explained by internal structures in the aster. Indeed, given the high density of astral microtubules, and their association with endomembranes such as the endoplasmic reticulum[15], an aster may be viewed as a sphere with low permeability[32,33]. The frictional coefficient of asters is thus expected be close to that of a non-permeable counterpart, and much smaller than the sum of the drag of individual microtubules. One possible source for such a large frictional coefficient is the confinement set by the cell boundary: the hydrodynamic interaction between the aster and cell boundaries could significantly reduce the hydrodynamic mobility of the aster. In support of this, recent quantitative hydrodynamic simulations suggest that even a moderate cell-confinement (aster/cell size~0.5) can lead to a 10–30 times increase of aster frictional coefficient[33]. Our experimental results may thus highlight the overlooked physical effect of cell-confinement on the mobility of intracellular structures.

Finally, we propose a simple model which explains how measured mechanical properties may account for aster positional fluctuations. Aster motion kinetics can be represented by one length-scale defined by dividing the diffusion coefficient by the mean speed, $D_x/V_x = 20\,\mathrm{nm}$. This small length-scale reflects the high persistency of aster motion. To illustrate how this characteristic length-scale may emerge from aster mechanics, we introduce a simple model for aster longitudinal motion (Fig. 4 and Supplementary Information). In this model, a single force-generation event created by a moving dynein on a microtubule causes a fixed aster displacement, δ_d, towards or away from the cell centre. We assume that force-generation obeys a first-order reaction, (that is, it is limited by either the binding or the activation of dynein), with a reaction rate K_f (K_r) proportional to the front (rear) aster radius L_f (L_r). Using Poisson statistics[34], we can express δ_d as a function of D_x/V_x as (see Supplementary Information):

$$\delta_d = \frac{2D_x}{V_x}\frac{K_f - K_r}{K_f + K_r} \qquad (3)$$

Assuming force balance between the aster and a single dynein-cargo complex, and using typical cargo vesicle parameters[11] (radius r ~ 0.5 µm and run-length l ~ 5 µm) and aster shape asymmetry[11] L_r/L_f ~ 0.8, this model predicts an aster hydrodynamic radius as $R = lr/\delta_d$ ~620 µm, which is comparable to our direct measurement of ~440 µm. This result demonstrates how the large aster frictional coefficient may suppress the motion error caused by dynein active fluctuations.

Owing to unusually large endogenous forces and friction, aster centration in large cells of early embryos is thus extremely precise, significantly more so than in well-controlled in vitro aster centration assays[4–6]. The large frictional coefficient enables asters to take an ensemble average of stochastic dynein force-generation events and ensures motion persistency. The transverse feedback further suppresses those fluctuations and can even bring the aster back along its centring trajectory after accidental deviations larger than those caused by dynein fluctuations (Fig. 3). Most fertilizing embryos are associated with rotational flows, shape changes and other cytoplasmic re-organization[7]. Microtubule asters in early embryos may thus be equipped with near-optimal physical designs to stabilize their motion in such an unfavourable environment to rapidly and precisely target the geometrical centre of large cells.

Methods

Methods, including statements of data availability and any associated accession codes and references, are available at https://doi.org/10.1038/s41567-018-0154-4.

Received: 5 October 2017; Accepted: 24 April 2018;
Published online: 28 May 2018

References

1. Bornens, M. The centrosome in cells and organisms. *Science* **335**, 422–426 (2012).
2. Tang, N. & Marshall, W. F. Centrosome positioning in vertebrate development. *J. Cell Sci.* **125**, 4951–4961 (2012).
3. Mitchison, T. et al. Growth, interaction, and positioning of microtubule asters in extremely large vertebrate embryo cells. *Cytoskeleton (Hoboken)* **69**, 738–750 (2012).
4. Holy, T. E., Dogterom, M., Yurke, B. & Leibler, S. Assembly and positioning of microtubule asters in microfabricated chambers. *Proc. Natl Acad. Sci. USA* **94**, 6228–6231 (1997).
5. Faivre-Moskalenko, C. & Dogterom, M. Dynamics of microtubule asters in microfabricated chambers: the role of catastrophes. *Proc. Natl Acad. Sci. USA* **99**, 16788–16793 (2002).
6. Laan, L. et al. Cortical Dynein Controls Microtubule Dynamics to Generate Pulling Forces that Position Microtubule Asters. *Cell* **148**, 502–514 (2012).
7. Gilbert, S. *Developmental Biology* 9th edn (Sinauer Associates, Sunderland, MA, 2010).
8. Hamaguchi, M. S. & Hiramoto, Y. Analysis of the role of astral rays in pronuclear migration in sand dollar eggs by the colcemid-UV method. *Dev., Growth & Differ.* **28**, 143–156 (1986).
9. Kimura, A. & Onami, S. Computer simulations and image processing reveal length-dependent pulling force as the primary mechanism for *C. elegans* male pronuclear migration. *Dev. Cell* **8**, 765–775 (2005).
10. Longoria, R. A. & Shubeita, G. T. Cargo transport by cytoplasmic dynein can center embryonic centrosomes. *PLoS ONE* **8**, e67710 (2013).
11. Tanimoto, H., Kimura, A. & Minc, N. Shape-motion relationships of centering microtubule asters. *J. Cell Biol.* **212**, 777–787 (2016).
12. Wuhr, M., Tan, E. S., Parker, S. K., Detrich, H. W. III, & Mitchison, T. J. A model for cleavage plane determination in early amphibian and fish embryos. *Curr. Biol.* **20**, 2040–2045 (2010).
13. Kimura, K. & Kimura, A. Intracellular organelles mediate cytoplasmic pulling force for centrosome centration in the *Caenorhabditis elegans* early embryo. *Proc. Natl Acad. Sci. USA* **108**, 137–142 (2011).
14. Terasaki, M. & Jaffe, L. A. Organization of the sea urchin egg endoplasmic reticulum and its reorganization at fertilization. *J. Cell Biol.* **114**, 929–940 (1991).
15. Minc, N., Burgess, D. & Chang, F. Influence of cell geometry on division-plane positioning. *Cell* **144**, 414–426 (2011).
16. Pierre, A., Salle, J., Wuhr, M. & Minc, N. Generic theoretical models to predict division patterns of cleaving embryos. *Dev. Cell* **39**, 667–682 (2016).
17. Haupt, A. & Minc, N. How cells sense their own shape - mechanisms to probe cell geometry and their implications in cellular organization and function. *J. Cell Sci.* **131**, jcs214015 (2018).
18. Wuhr, M., Dumont, S., Groen, A. C., Needleman, D. J. & Mitchison, T. J. How does a millimeter-sized cell find its center? *Cell Cycle* **8**, 1115–1121 (2009).

19. Zhu, J., Burakov, A., Rodionov, V. & Mogilner, A. Finding the cell center by a balance of dynein and myosin pulling and microtubule pushing: a computational study. *Mol. Biol. Cell* **21**, 4418–4427 (2010).
20. Fulton, A. B. How crowded is the cytoplasm? *Cell* **30**, 345–347 (1982).
21. Brangwynne, C. P., Koenderink, G. H., MacKintosh, F. C. & Weitz, D. A. Cytoplasmic diffusion: molecular motors mix it up. *J. Cell Biol.* **183**, 583–587 (2008).
22. Winkler, F. et al. Fluctuation analysis of centrosomes reveals a cortical function of Kinesin-1. *Biophys. J.* **109**, 856–868 (2015).
23. Pecreaux, J. et al. The mitotic spindle in the one-cell *C. elegans* embryo is positioned with high precision and stability. *Biophys. J.* **111**, 1773–1784 (2016).
24. Almonacid, M. et al. Active diffusion positions the nucleus in mouse oocytes. *Nat. Cell Biol.* **17**, 470–479 (2015).
25. Garzon-Coral, C., Fantana, H. A. & Howard, J. A force-generating machinery maintains the spindle at the cell center during mitosis. *Science* **352**, 1124–1127 (2016).
26. Hamaguchi, M. S., Hamaguchi, Y. & Hiramoto, Y. Microinjected polystyrene beads move along astral rays in sand dollar eggs. *Dev. Growth Differ.* **28**, 461–470 (1986).
27. Shinar, T., Mana, M., Piano, F. & Shelley, M. J. A model of cytoplasmically driven microtubule-based motion in the single-celled *Caenorhabditis elegans* embryo. *Proc. Natl Acad. Sci. USA* **108**, 10508–10513 (2011).
28. Barbosa, D. J. et al. Dynactin binding to tyrosinated microtubules promotes centrosome centration in *C. elegans* by enhancing dynein-mediated organelle transport. *PLoS Genet.* **13**, e1006941 (2017).
29. Grill, S. W., Howard, J., Schaffer, E., Stelzer, E. H. & Hyman, A. A. The distribution of active force generators controls mitotic spindle position. *Science* **301**, 518–521 (2003).
30. De Simone, A., Spahr, A., Busso, C. & Gonczy, P. Uncovering the balance of forces driving microtubule aster migration in *C. elegans* zygotes. *Nat. Commun.* **9**, 938 (2018).
31. Hiramoto, Y. Mechanical properties of the protoplasm of the sea urchin egg. II. *Fertil. Egg. Exp. Cell Res* **56**, 209–218 (1969).
32. Nazockdast, E., Rahimian, A., Needleman, D. & Shelley, M. Cytoplasmic flows as signatures for the mechanics of mitotic positioning. *Mol. Biol. Cell* **28**, 3261–3270 (2017).
33. Nazockdast, E., Rahimian, A., Zorin, D. & Shelley, M. A fast platform for simulating semi-flexible fiber suspensions applied to cell mechanics. *J. Comput. Phys.* **329**, 173–209 (2017).
34. Svoboda, K., Mitra, P. P. & Block, S. M. Fluctuation analysis of motor protein movement and single enzyme kinetics. *Proc. Natl Acad. Sci. USA* **91**, 11782–11786 (1994).

Acknowledgements

The authors acknowledge M. Coppey and J. Azimzadeh for technical support, and S. Dmitrieff, T. Strick, M. Piel, M. Thery and K. Laband for careful reading of the manuscript. This research was supported by the CNRS and grants from the 'Mairie de Paris emergence' program, the FRM 'amorçage' grant AJE20130426890 and the European Research Council (CoG Forcaster N° 647073).

Author contributions

H.T., L.D., J.S. and N.M. performed experiments. H.T. analysed the data and developed the model. H.T. and N.M. designed the research and wrote the manuscript.

Competing interests

The authors declare no competing interests.

Additional information

Supplementary information is available for this paper at https://doi.org/10.1038/s41567-018-0154-4.

Reprints and permissions information is available at www.nature.com/reprints.

Correspondence and requests for materials should be addressed to N.M.

Publisher's note: Springer Nature remains neutral with regard to jurisdictional claims in published maps and institutional affiliations.

Methods

Sea urchin gametes. Purple sea urchins (*Paracentrotus lividus*) were obtained from either L'Oursine de Ré or the Roscoff Marine station, and maintained in aquariums. Artificial sea water (ASW; Reef Crystals, Instant Ocean) was used for adult maintenance in aquariums and embryo development. Gametes were collected by intracoelomic injection of 0.5 M KCl. Dry sperm was kept at 4 °C and used within 1 week. Eggs were rinsed twice with ASW, kept at 16 °C, and used on the day of collection.

High-speed aster centration imaging. Aster centration imaging was performed as described in ref. [11]. Briefly, eggs were first passed three times through a 80-µm Nitex mesh, incubated for 30 min with 10 µg ml^{-1} Hoechst 33342 (Sigma-Aldrich) and subsequently allowed to sediment and stick on protamine-coated glass chambers. An activated sperm solution was prepared by diluting the sperm stock 1000× in ASW with subsequent vigorous up and down motion with a Pasteur pipette. One drop of this solution was added to the dish for fertilization. The centre of sperm microtubule asters was tracked by visualizing the Hoechst-stained DNA of the male pro-nucleus.

Time-lapses were acquired on a spinning-disk confocal microscope (TI-Eclipse, Nikon) equipped with a Yokogawa CSU-X1FW spinning head, and an EM-CCD camera (Hamamatsu), using a 60× oil-immersion objective (Apo, NA 1.4, Nikon). The pixel size was 0.180 µm. The microscope was operated by MetaMorph (Molecular Devices), using a high-speed image acquisition in 'stream' mode. The imaging area was reduced to obtain a frame rate of 20 Hz.

After fertilization, an egg in which the sperm entered close to the equatorial plane was selected. Image acquisition was then started after the aster had moved 10–15 µm from the cell boundary, and monitored for 3–5 min at 20 Hz, corresponding to 3,600–6,000 time frames. Motion in Z was evaluated based on the focus quality of the Hoechst signal. Samples exhibiting large Z motion were excluded from the analysis. Imaged eggs proceeded to subsequent cell division and development.

Pharmacological inhibitors. Cytoskeletal inhibitors were applied by rapidly exchanging the medium in chambers. Drugs were applied after asters had migrated about 10 µm away from the cell boundary (typically ~ 5 min post fertilization). High-speed imaging was initiated 1–2 min after inhibitor application. Inhibitors were prepared in 100× stock aliquots in dimethyl sulfoxide (DMSO). Latrunculin B (Sigma-Aldrich) was used at a final concentration of 20 µM, Nocodazole (Sigma-Aldrich) at a final concentration of 20 µM and Ciliobrevin D (EMD Millipore) at a concentration of 100 µM.

High-resolution tracking. The sub-pixel localization of the centre of the aster was obtained using standard analysis methods involving two-dimensional (2D) Gaussian fits. An 80×80 pixel area was cropped around the aster center and used for successive analysis (Supplementary Fig. 1a,b). The intensity profile of the Hoechst signal was fitted with a 2D Gaussian function, and the aster centre was defined as the mode of the best-fit Gaussian (Supplementary Fig. 1c,d). The spatial resolution was evaluated to be around 20 nm, by performing those analyses in fixed samples (Supplementary Fig. 1e,f). The effect of DNA signal deformation was mostly negligible when compared to the net displacement of asters (Supplementary Fig. 1e).

Fluctuation analyses. XY coordinates for the fluctuation analyses were defined by aligning the X axis with the longitudinal centring direction. Previous studies showed that aster centration in this system is persistent, with a large fraction of the centration motion associated with an average constant directionality and speed[11]. Therefore, the XY coordinates were defined by assuming no systematic drift in the transverse Y axis—that is, a temporal integration of the Y position equal to zero. The outputs of the analyses did not depend on the particular choice of the coordinate origin, which was thus set to be the initial position of the aster centre.

The aster trajectory $\mathbf{X}(t) = (X(t), Y(t))$ can be decomposed into a deterministic component with constant velocity $\mathbf{V}$ and a stochastic component $\mathbf{d}(t)$, as

$$\mathbf{X}(t) = \mathbf{V}t + \mathbf{d}(t) \tag{4}$$

To separate those two components, the residual displacement of the aster centre, $\delta\mathbf{X} = (\delta X,\ \delta Y)$, was defined using a linear detrend of aster trajectory[22] (Supplementary Fig. 1g):

$$\delta\mathbf{X}(t;\delta t) \equiv \mathbf{X}(t) - \frac{1}{2}(\mathbf{X}(t+\delta t) + \mathbf{X}(t-\delta t)) \tag{5}$$

Putting equation S1 into equation 5, yields

$$\delta\mathbf{X}(t;\delta t) = \mathbf{d}(t) - \frac{1}{2}(\mathbf{d}(t+\delta t) + \mathbf{d}(t-\delta t)) \tag{6}$$

in which $\mathbf{V}$ vanishes, indicating that $\delta\mathbf{X}$ may be regarded as the positional fluctuation accumulated during the lag time δt. The amplitude of $\delta\mathbf{X}(t;\delta t)$ for a fixed δt was mostly constant during the measurement period, suggesting that aster positional fluctuation can be considered as a steady-state problem (Supplementary Fig. 2).

The statistical properties of positional fluctuations were characterized by computing the mean-squared residual displacements (MSrD) along the X and Y axes; $\mathrm{MSrD}_x(\delta t) \equiv \langle \delta X^2(t;\delta t) \rangle_t$, $\mathrm{MSrD}_y(\delta t) \equiv \langle \delta Y^2(t;\delta t) \rangle_t$, where $\langle\rangle_t$ denotes temporal average. The 1D diffusion coefficient along the X axis, D_x, was determined by linear fitting of $\mathrm{MSrD}_x(\delta t)$ for the period up to δt=35 sec. D_y and the saturation timescale of fluctuations along the Y-axis, τ, were determined by fitting $\mathrm{MSrD}_y(\delta t)$ for the period up to 60 sec using

$$\mathrm{MSrD}_y(\delta t) = 2\tau D_y(1 - e^{-\delta t/\tau}) \tag{7}$$

which describes a random walk of inertia-free particles under spring-like restoration forces[35]. Equation 7 shows that the Y fluctuation is bound by $2\tau D_y$, which corresponds to the saturated Y fluctuation amplitude for the longer timescale.

Magnetic tweezers set-up. The magnet tip used for force applications in vivo was built from three rod-shaped strong neodymium magnets (diameter 4 mm, height 10 mm, S-04-10-AN supermagnet) prolonged by a sharpened steel piece with a tip radius of ~50 µm to create a magnetic gradient.. The surface of the steel tip was electro-coated with gold to prevent oxidization.

The magnetic tweezers were mounted on an inverted epifluorescent microscope (TI-Eclipse, Nikon) combined with a complementary metal–oxide–semiconductor (CMOS) camera (Hamamatsu). Eggs were filmed with a 20× dry objective (Apo, NA 0.75, Nikon) and a 1.5× magnifier, yielding a pixel size of 0.217 µm. The microscope was operated with Micro-Manager (Open Imaging). The magnetic tweezers were controlled using a micromanipulator (Injectman 4, Eppendorf).

Magnetic beads. To apply magnetic forces to intact sperm microtubule asters in eggs, several types of magnetic beads were tested. Large 2.8-µm-diameter beads, allowed the application of large and localized forces, but did not strongly attach to asters (Supplementary Fig. 5). On the other hand, small super-paramagnetic beads (NanoLink, solulink) (beads diameter 150–800 nm) had several advantages for the force experiments. First, it was possible to inject many beads without damaging the eggs. Second, injected beads were transported towards the aster centre, most likely along astral microtubules in a dynein- and microtubule-dependent manner (Supplementary Fig. 6a)[26]. This natural centripetal motion strongly facilitated the targeting process. The beads usually formed a single large aggregate stably attached to the aster centre, which enabled the application of large forces to asters.

To prepare beads for injection, a solution of 10 µl of undiluted streptavidin-beads was first washed in 100 µL of washing solution (1 M NaCl with 1% Tween-20), and sonicated for 5 min. Beads were then washed three times in water and re-suspended in 20 µL of Atto-488-biotin solution to render them fluorescent for 30 min at room temperature, and then kept on ice until use.

Unfertilized eggs were placed on protamine-coated glass bottom dish. The bead solution was injected using a micro-injection system (FemtoJet 4, Eppendorf) and a micro-manipulator (Injectman 4, Eppendorf). Injection pipettes were prepared from siliconized (Sigmacote) borosilicate glass capillaries (1 mm diameter). Glass capillaries were pulled using a needle puller (P-1000, Sutter Instrument) and ground with a 30° angle on a diamond grinder (EG-40, Narishige) to obtain a 10 µm aperture. Injection pipettes were back-loaded with 2 µl of bead solution before each experiment, and were not re-used.

After injection, beads were accumulated on the egg side with the magnet, and subsequently released. Following fertilization, beads were naturally transported close to the male pro-nucleus at the centre of the sperm aster, where they formed a large aggregate. Beads targeting was often aided by approaching the magnet (Supplemetary Movie S2).

The tight binding of the beads to the aster centre was assessed by monitoring the distance between the beads aggregate and the Hoechst-stained sperm pro-nucleus at the aster centre. This distance was mostly constant during force application (Supplementary Fig. 8), suggesting a tight binding between beads and asters. In the presence of 20 µM Nocodazole or 100 µM Ciliobrevin D, beads detached from the aster under external forces and rapidly moved in the cytoplasm. Beads also occasionally detached from the aster during force application (Supplementary Fig. 6c). The mobility of those detached beads was comparable to beads detaching in the presence of Nocodazole or Ciliobrevin D, and significantly larger than that of the beads-aster complex (Supplementary Fig. 6d).

Immunostaining. Immunostaining was performed using similar procedures as described previously[11]. Fixation to control for the effect of Ciliobrevin D was done in bulk, as described in Supplementary Fig 3. The fixation of eggs with injected beads was performed in injection dishes after bead injection, fertilization and bead targeting to the aster centre (Supplementary Fig 9a). Fixations were done under the microscope to ensure that eggs did not move or change shape during liquid exchange. Eggs were first fixed for 70 min in 100 mM Hepes, pH 6.9, 50 mM EGTA, 10 mM $MgSO_4$, 2% formaldehyde, 0.2% glutaraldehyde, 0.2% Triton X-100

and 400 mM glucose. Eggs were then rinsed three times for 10 min in phosphate buffered saline (PBS) plus Tween 20 (PBT) and one time in PBS, then placed in 0.1% $NaBH_4$ in PBS made fresh for 30 min. Eggs were rinsed again with PBS and PBT and blocked in PBT plus 5% goat serum and 0.1% bovine serum albumin (BSA) for 30 min. For microtubule staining, cells were incubated for 48 h with a primary anti–α-tubulin antibody, clone DM 1 A (Sigma-Aldrich) at 1/8,000, rinsed twice in PBS, and then incubated for 4 h with fluorophore-conjugated anti-mouse secondary antibody (Sigma-Aldrich) at 1/750.

Magnetic force calibration. To calibrate magnetic forces, we first characterized the large-scale magnetic force field created by the magnet tip. To this aim, 2.8 µm mono-dispersed magnetic beads were placed in a viscous test fluid (80% glycerol, viscosity 8.0×10^{-2} Pa sec at 22°C) and pulled by the same magnet as used in vivo along its principal axis (Supplementary Fig. 8a). The motion of the fluid during the force application was measured using non-magnetic tracer beads and found to be largely negligible. The speed of a bead, which is proportional to the magnetic force, was finally plotted as a function of the distance between the bead and the magnet tip (Supplementary Fig. 8b).

Next, we characterized the drag coefficients of the bead aggregates. To form aggregates in vitro, magnetic beads were first washed and labelled following the above-mentioned protocol. 10 µL of beads were then mixed with 100 µL Poly-L-Lysine (1 mg mL^{-1}) and incubated for 3 min. This caused beads to form aggregates with sizes ranging from 2 to 8 µm, typically similar to what is observed in cells (Supplementary Fig. 8c). Those aggregates were tightly packed and largely homogenous, similar to the aggregates formed inside cells (Supplementary Fig. 7a-h) We also confirmed that, for both in vitro and in vivo situations, the aggregates did not largely change their size in the presence of magnetic fields (Supplementary Fig. 7i,j). The data suggest that aggregates prepared in vitro are close to those formed in the cell.

Aggregates prepared in vitro were placed in 50% glycerol (viscosity 7.7×10^{-3} Pa sec at 22 °C) between a glass slide and a coverslip and allowed to sediment. The fall speed was measured by acquiring a Z-stack in time-lapse with a spinning-disk confocal microscope (Supplementary Fig. 8d). The Z interval used was 3 µm and the time interval was 5 sec. The signal intensity of the beads in each Z planes was plotted as a function of Z, and the position of the aggregate centre was determined as the mode of a best-fit Gaussian for the intensity profile along the Z axis. (Supplementary Fig. 8e). The fall speed of aggregations was determined by the linear fit of a Z position–time plot (Supplementary Fig. 8f).

We found that the fall speed of aggregates was well approximated by that of a sphere with the same size (Supplementary Fig. 8g). The fall speed of a perfect sphere with radius R follows the Stokes' law so that

$$V=\frac{2(\rho_{\text{beads}}-\rho_{\text{solution}})g}{9\eta}R^2 \qquad \text{(S5)}$$

where η is the viscosity of the test fluid, and ρ_{beads} (ρ_{solution}) is the density of beads (test fluid). The size of the aggregate R_a was defined using the longest length L_1 and the length perpendicular to the longest axis, L_2, as $R_a=\sqrt{L_1L_2}/2$. The fall speed of the aggregates was slightly but consistently smaller than that of a sphere with the same size, which is expected since the drag at low Reynolds number is governed by the largest dimension of an object[36]. We evaluated this effect by fitting the results with $V=\alpha R_a^2$, where α is a fitting parameter. The best fit gave $\alpha=0.66$.

We then pulled the bead aggregates in 80% glycerol and measured the speed V (Supplementary Fig. 8h,i). The speed was translated into a force using Stokes' law $F=6\pi\eta R_aV$, approximating aggregates as a sphere of radius R_a. Our direct measurement indicates that this approximation can lead to a ~35% underestimation of the magnetic force. This analysis allowed the computation of the magnetic force at a fixed distance (100 µm) as a function of aggregate size (Supplementary Fig. 8i). The force–size relationship was well described by a cubic function, consistent with a magnetic dipole proportional to the aggregate volume. These force–size and force–distance relationships of the bead aggregates were used to compute the magnetic forces applied to asters inside cells.

Magnetic force applications inside eggs. Unfertilized eggs were placed on a protamine-coated glass bottom dish (P50G-0-14-F, MatTek), as described above. About 20 eggs were micro-injected with magnetic beads and fertilized under the microscope. An egg in which a sperm entered at the equatorial plane and close to the beads was selected. The dish was then rotated to align the force direction and the principal axis of the magnetic tweezers. The centre of the aster was tracked using the Hoechst-stained male pro-nucleus. Bead aggregates were tracked either in differential interference contrast (DIC) or using fluorescence. Time-lapse movies were acquired with a time interval of 10 sec.

The force amplitude was controlled by adjusting the longitudinal position of the magnet tip. It took less than the time interval (10 sec) to modify the position of the magnet. The positions of the magnet tip and aster centre were recorded in DIC and fluorescence, respectively. The distance between the aster and the beads was computed to control for the tight binding between the aster and the beads in each experiment.

Data analysis 1. Force applications along the centration axis. In experiments in which the forces were applied along the centring longitudinal direction of the aster, the force amplitude was varied 1–4 times in a step-like manner during each experiment. To minimize possible contributions from aster adaptive responses, we focused on short-time changes in aster speed. To that aim, we selected and analysed typically four time points (30 sec) in each force step application, during which the aster velocity and beads–aster distance were constant in time. The magnetic forces were computed using the beads–magnet tip distance at the mid-time point, which corresponds to an average force amplitude for the force application period. Aster velocity was defined using a linear fit of the aster trajectory. In front-pull experiments, asters sometimes overran the cell centre when we applied the magnetic force for a long time (see Supplementary Fig. 10 Cell #11, for an example). These periods were excluded from the analysis. Importantly, aster frictional coefficient and stall force values were not grossly affected when considering only the first force step application, or all subsequent steps; ruling out dramatic aster reorganization after force applications. Finally, those parameters were also mostly robust to the range of aggregate sizes used (Supplementary Fig. 12).

Data analysis 2. Force applications orthogonal to the centration axis. In experiments in which forces were applied along the axis transverse to centration, the asters were pulled until their Y position reached saturation, which took typically 1–2 min. In the force–displacement analyses, the magnetic forces were computed using the distance between the magnet tip and bead aggregates at the end of the force application where aster Y position reached saturation. The centration axis was defined in a semi-automated manner, using the trajectory before force application.

The recovery dynamics of the transverse Y position after force cessation was fitted using

$$Y(t)-Y_\infty=Y(0)e^{-t/\tau_r} \qquad \text{(S6)}$$

where t=0 corresponds to the time of force cessation. The recovery time-scale τ_r did not depend on the Y saturation (Fig. 3d, inset), suggesting that the aster response is in a linear regime.

Additional information. The experimental protocol was approved by Isabelle Le Parco, head of the animal facility at Institut Jacques Monod.

Reporting Summary. Further information on experimental design is available in the Nature Research Reporting Summary linked to this article.

Data Availability Statement. The data that support the plots within this paper and other findings of this study are available from the corresponding author upon request.

References

35. Doi, M. & Edwards, S. F. *The Theory of Polymer Dynamics* Vol. 73 (Oxford Univ. Press, Oxford, 1988).
36. Happel, J. & Brenner, H. *Low Reynolds Number Hydrodynamics: With Special Applications to Particulate Media* Vol. 1 (Springer, The Hague 2012).

nature research

Corresponding author(s): Nicolas MINC

Reporting Summary

Nature Research wishes to improve the reproducibility of the work that we publish. This form provides structure for consistency and transparency in reporting. For further information on Nature Research policies, see Authors & Referees and the Editorial Policy Checklist.

Statistical parameters

When statistical analyses are reported, confirm that the following items are present in the relevant location (e.g. figure legend, table legend, main text, or Methods section).

n/a	Confirmed	
☐	☒	The exact sample size (*n*) for each experimental group/condition, given as a discrete number and unit of measurement
☐	☒	An indication of whether measurements were taken from distinct samples or whether the same sample was measured repeatedly
☐	☒	The statistical test(s) used AND whether they are one- or two-sided *Only common tests should be described solely by name; describe more complex techniques in the Methods section.*
☒	☐	A description of all covariates tested
☐	☒	A description of any assumptions or corrections, such as tests of normality and adjustment for multiple comparisons
☐	☒	A full description of the statistics including central tendency (e.g. means) or other basic estimates (e.g. regression coefficient) AND variation (e.g. standard deviation) or associated estimates of uncertainty (e.g. confidence intervals)
☐	☒	For null hypothesis testing, the test statistic (e.g. *F*, *t*, *r*) with confidence intervals, effect sizes, degrees of freedom and *P* value noted *Give P values as exact values whenever suitable.*
☒	☐	For Bayesian analysis, information on the choice of priors and Markov chain Monte Carlo settings
☐	☒	For hierarchical and complex designs, identification of the appropriate level for tests and full reporting of outcomes
☐	☒	Estimates of effect sizes (e.g. Cohen's *d*, Pearson's *r*), indicating how they were calculated
☐	☒	Clearly defined error bars *State explicitly what error bars represent (e.g. SD, SE, CI)*

Our web collection on statistics for biologists may be useful.

Software and code

Policy information about availability of computer code

Data collection	Data Collection was performed using Micromanager and/or Metamorph
Data analysis	All data analysis was done with custom code written in MATLAB R2013a.

For manuscripts utilizing custom algorithms or software that are central to the research but not yet described in published literature, software must be made available to editors/reviewers upon request. We strongly encourage code deposition in a community repository (e.g. GitHub). See the Nature Research guidelines for submitting code & software for further information.

Data

Policy information about availability of data

All manuscripts must include a data availability statement. This statement should provide the following information, where applicable:

- Accession codes, unique identifiers, or web links for publicly available datasets
- A list of figures that have associated raw data
- A description of any restrictions on data availability

The data that support the plots within this paper and other findings of this study are available from the corresponding author upon request.

Field-specific reporting

Please select the best fit for your research. If you are not sure, read the appropriate sections before making your selection.

☒ Life sciences ☐ Behavioural & social sciences

For a reference copy of the document with all sections, see nature.com/authors/policies/ReportingSummary-flat.pdf

Life sciences

Study design

All studies must disclose on these points even when the disclosure is negative.

Sample size	The sample size was determined so that both the variance of the data and standard error of the model fitting are reasonably small.
Data exclusions	For the fluctuation analysis, we excluded data for which we loose the focus during the measurements. For the force measurement, we excluded data for which we could not maintain the constant force for sufficiently long time.
Replication	All experiments were performed at least twice and reliably reproduced.
Randomization	We used gametes of sea urchins and randomly selected for all experiments.
Blinding	All data were analyzed in an automated manner.

Materials & experimental systems

Policy information about availability of materials

n/a	Involved in the study
☒	☐ Unique materials
☐	☐ Antibodies
☒	☐ Eukaryotic cell lines
☐	☐ Research animals
☒	☐ Human research participants

Antibodies

Antibodies used	Primary anti–α-tubulin antibody, clone DM 1A (Sigma-Aldrich) Anti-mouse secondary antibody (Sigma-Aldrich)
Validation	Those are antibodies which have been validated in multiple species , including Sea urchin embryos, by the Manufacturer and other scientists

Research animals

Policy information about studies involving animals; ARRIVE guidelines recommended for reporting animal research

Animals/animal-derived materials	Paracentrotus lividus (obtained from either L'Oursine de Ré or the Roscoff Marine station)

Method-specific reporting

n/a	Involved in the study
☒	☐ ChIP-seq
☒	☐ Flow cytometry
☒	☐ Magnetic resonance imaging